

CANCER

Eradication of tumor growth by delivering novel photothermal selenium-coated tellurium nanoheterojunctions

Shiyu Chen^{1,2,3*}, Chenyang Xing^{1,4*}, Dazhou Huang¹, Chuanhong Zhou¹, Bo Ding⁵, Ziheng Guo⁶, Zhengchun Peng⁴, Dou Wang³, Xi Zhu⁷, Shuzhen Liu⁸, Zhen Cai⁹, Jieyu Wu², Jiaqi Zhao³, Zongze Wu³, Yuhua Zhang³, Chaoying Wei³, Qiaoting Yan³, Hongzhong Wang³, Dianyuan Fan¹, Liping Liu^{3†}, Han Zhang^{1†}, Yihai Cao^{2†}

Two-dimensional nanomaterial-based photothermal therapy (PTT) is currently under intensive investigation as a promising approach toward curative cancer treatment. However, high toxicity, moderate efficacy, and low uniformity in shape remain critical unresolved issues that hamper their clinical application. Thus, there is an urgent need for developing versatile nanomaterials to meet clinical expectations. To achieve this goal, we developed a stable, highly uniform in size, and nontoxic nanomaterials made of tellurium-selenium (TeSe)-based lateral heterojunction. Systemic delivery of TeSe nanoparticles in mice showed highly specific accumulation in tumors relative to other healthy tissues. Upon exposure to light, TeSe nanoparticles nearly completely eradicated lung cancer and hepatocellular carcinoma in preclinical models. Consistent with tumor suppression, PTT altered the tumor microenvironment and induced immense cancer cell apoptosis. Together, our findings demonstrate an exciting and promising PTT-based approach for cancer eradication.

INTRODUCTION

Nanomaterials are emerging therapeutic approaches for effective treatment of various cancers (1), and their therapeutic mechanisms are multifarious, including photothermal agents (2–4), photodynamic agents (5), drug release platforms (6), and photoacoustic imaging (PAI) enhancers (7, 8). Two-dimensional (2D) nanomaterials have attracted great attention for medical applications owing to their beneficial potentials for disease diagnosis and therapy. They may also be used in combination with different therapeutic modalities such as photothermal therapy (PTT), drug delivery, and photodynamic therapy (PDT) (9). Light-sensitive nanomaterials such as black phosphorus (BP) exhibit a synergistic antitumor effect by releasing photothermal energy and chemotherapeutic agents (10, 11). Another example is Ti₃C₂ MXene serving as a theranostic agent by combining PTT and PAI (6, 12). Other 2D nanomaterials, such as reduced graphene oxide (rGO) (13) and transition metal dichalcogenides (14), have been applied in various therapeutic settings.

Emerging 2D nanomaterials that have improved biocompatibility, higher photothermal effects, and additional simultaneous functionalities depict a promising future for biomedical applications. However, several challenging issues in this field remain to be resolved before clinical use in human patients (15). First, biosafety is the absolute prerequisite for clinical development (16), including short-term and long-term safety concerns (17, 18). Short-term toxicity is often caused by directly inducing cellular dysfunction and manifests acute clinical symptoms. The long-term toxicity may experience a latent symptom-free period but manifests symptoms over a long period of time by accumulating nanomaterials in the affected tissues and organs (19, 20). In most cases, these adverse effects can be alleviated by lowering dosages, albeit compromising therapeutic efficacy. Second, high therapeutic efficacy over the existing modalities or synergistic efficacy in combination with conventional therapy should be achieved. As for light-sensitive nanomaterials, in addition to light intensity, therapeutic efficacy can be controlled by the nanomaterial performance, i.e., light absorbance, light-to-heat conversion efficiency, and the targeting efficiency to specific pathological tissues such as tumors (21). Third, nanomaterials for clinical use should be homogeneous and ideally exert identical or at least similar functions in all patients with cancer (22). For 2D nanomaterials to meet these prerequisites, shape uniformity is crucial to ensure consistent nanomaterial properties from each fabricated batch. Last, stability and biodegradability are additional important factors to meet pharmacokinetics within the therapeutic window (23, 24). A high degree of stability ensures long-lasting beneficial effects, whereas continuous biodegradability ensures biocompatibility and biosafety. An ideal therapeutic nanomaterial should have a pharmacokinetic balance between stability and degradation, maximizing therapeutic efficacy and minimizing adverse effects.

Although many existing 2D nanomaterials are multifunctional, they exhibit various degrees of inadequacies for cancer therapy in human patients. One of the common defective properties is the lack

¹Shenzhen Engineering Laboratory of Phosphorene and Optoelectronics, International Collaborative Laboratory of 2D Materials for Optoelectronics Science and Technology of Ministry of Education, College of Physics and Optoelectronic Engineering, Shenzhen University, Shenzhen 518060, P.R. China. ²Department of Microbiology, Tumor and Cell Biology, Karolinska Institutet, Stockholm 171 77, Sweden. ³Department of Hepatobiliary and Pancreatic Surgery, Shenzhen People's Hospital, The First Affiliated Hospital of Southern University of Science and Technology, Shenzhen 518020, Guangdong, P.R. China. ⁴Center for Stretchable Electronics and Nanoscale Systems, Key Laboratory of Optoelectronic Devices and Systems of Ministry of Education, College of Physics and Optoelectronic Engineering, Shenzhen University, Shenzhen 518060, P.R. China. ⁵Department of Respiratory Disease, The Fourth Hospital of Jinan, Jinan, Shandong 250031, P.R. China. ⁶Department of Pancreatic Surgery, West China School of Medicine, Sichuan University, Chengdu, P.R. China. ⁷School of Science and Engineering, The Chinese University of Hong Kong, Shenzhen, Shenzhen 518172, P.R. China. ⁸Weifang People's Hospital, Weifang 261041, P.R. China. ⁹Fuwai Hospital Chinese Academy of Medical Sciences, Shenzhen, Shenzhen 518000, Guangdong Province, P.R. China.

*These authors contributed equally to this work.

†Corresponding author. Email: yihai.cao@ki.se (Y.C.); hzhang@szu.edu.cn (H.Z.); liu.liping@szhospital.com (L.L.)

of shape uniformity of most liquid phase–exfoliated 2D nanomaterials (25, 26). For the carbon-based graphene and rGO, low efficiency of light-to-heat conversion leads to poor therapeutic potentials and compensatory high dosage that may result in overt adverse effects (27). BP instability has both advantages and disadvantages for therapeutic development, i.e., advantageous nontoxicity and difficulties of fabrication and storage (28). While for another 2D nanomaterial, antimonene, although stable in air (29), its instability in water can cause toxicity. On the basis of urgent medical needs for clinical development, we have developed an upgraded PTT-based anticancer therapy using tellurium-selenium (TeSe)–made nanomaterial.

Tellurium, a member of the chalcogen family, is an important element in manufacturing industrial instruments. Over past decades, various Te nanostructures have been fabricated, including hydrothermal and solvothermal methods, liquid-phase exfoliation, reflux processes, template-based strategies, and vacuum vapor deposition (30). By using rationally designed strategies, Te nanomaterials with different morphologies were fabricated. Among all these structures, only a few were successfully deployed in the biomedical field. Te nanorods and nanodots were reported to achieve simultaneous chemophotothermal combination cancer therapy, demanding tight capping by polysaccharide proteins, human serum albumin, and an extremely high power density (28, 31). Recently, Lin *et al.* (32) reported that 2D tellurium nanosheets could be developed for PAI-guided PDTs after the capping of glutathione to prevent tellurium oxidation. Although stable in air, tellurium nanomaterials are often unstable in water and other solvents (33). Furthermore, the degradation-associated products are often toxic by forming stress granules in cells (34).

In the present study, we fabricated a novel 2D lateral heterojunction, i.e., selenium-coated tellurium nanoheterojunctions. The newly synthesized TeSe was stable, biocompatible, and uniform in shape with marked tumor-targeting and antitumor effects. We show anticancer efficacy of TeSe nanomaterials, beneficial mechanisms, and their impact on alteration of the tumor microenvironment (TME).

RESULTS

Morphological characterization

The TeSe nanomaterials were synthesized via a hydrothermal reaction route. In a typical synthetic process, the Na_2SeO_3 and Na_2TeO_3 precursors were reduced to TeSe-based nanomaterials in the presence of the $\text{N}_2\text{H}_4 \cdot \text{H}_2\text{O}$ reductant. Polyvinylpyrrolidone (PVP) was used as a crystal face–blocking ligand during the redox reaction. The impact of the initial molar ratio of Te (Na_2TeO_3) to Se (Na_2SeO_3) precursors (hereafter denoted as TeSe) on nanomaterial morphology was studied (Fig. 1). Notably, TeSe(1:0.25), TeSe(1:0.5), TeSe(1:0.75), and TeSe(1:1) produced oval-shaped 2D structures, as detected by transmission electron microscopy (TEM) images (Fig. 1, A to D). Higher-magnification TEM images of these samples showed that the TeSe nanostructures progressively decreased in size by increasing the Se ratio (Fig. 1, E to H, and fig. S1). A similar trend was observed at other PVP concentrations (fig. S2). In addition, altering the Te:Se ratio also influenced the morphology of the TeSe nanomaterials (fig. S2). The TeSe(1:0.25), TeSe(1:0.5), TeSe(1:0.75), and TeSe(1:1) samples were also characterized by atomic force microscopy (AFM) imaging (Fig. 1, I to L). All TeSe samples exhibited small 2D geometries, reconciling with their TEM micrographs. Clear stacking at the particle edges was observed (fig. S2). Therefore, the TeSe nanomaterials were considered as 2D materials. Furthermore, the

thickness of TeSe samples progressively decreased by increasing the Se ratio. For example, a thickness of ~ 33 nm was observed for TeSe(1:0.25), which was decreased to 23 to 27 nm at the ratios of 1:0.5 and 1:0.75, while at the TeSe ratio of 1:1, 19- to 24-nm particles were detected (Fig. 1M). Using Te:Se ratio of 1:1 as a standard, statistical analyses showed that change of Te:Se ratios significantly altered the thickness of nanoparticles (Fig. 1N and fig. S1C). Together, these results demonstrated that both lateral and vertical dimensions decreased with the increase of Te:Se ratio.

Physical property characterization

To better understand the morphology of the TeSe nanomaterials, we subjected double spherical aberration–corrected TEM for further analysis (Fig. 2). The elemental distribution (Te, Se, O, and C), averaged over partial sections of three nanoparticles, and the interstices between particles were analyzed for the TeSe(1:0.25) sample (Fig. 2A). Both Te and Se were detected (Fig. 2, B and C). The intensity of Te at the surface was stronger than that at the edge, and Se exhibited a stronger signal at the particle edge than surface (Fig. 2D). The Te-rich center was encircled by a Se ring, and O- and C-rich signals were observed (Fig. 2, E to G). High-resolution TEM (HRTEM) images revealed the atomic arrangements at the particle surfaces and amorphous regions at edge regions of particles (Fig. 2H). The HRTEM micrograph also showed clear interplanar spacing distances of 0.19 and 0.23 nm (Fig. 2I). Inductively coupled plasma atomic emission spectroscopy validated the TeSe weight percent values and PVP in the TeSe-based nanomaterials (table S1).

In the absence of Se, Te formed as nanowires (Fig. 2J), which were unstable in water and became degraded over a 2-day period (fig. S3). However, in the presence of Se, Te crystallized into particles with 2D geometry and highly chemical stability (fig. S3). Together with the PVP-tailed structures, the 2D oval-like TeSe morphology indicated that Se atoms shifted from Te 1D growth to 2D growth, generating 2D PVP-tailed TeSe nanostructures (Fig. 2J). Theoretical calculations supported the Te core–Se shell nanostructures (fig. S4). The oxidized atomic structures further conformed the Te core–Se shell configuration by 0.04 eV per Se atom during the oxidization process (Fig. 2, K and L, and fig. S4). Thus, the TeSe lateral heterojunction structures stabilized the pure Te nanomaterials and affected the light absorption.

The x-ray diffraction (XRD) patterns of bulk Te, bulk Se, and the TeSe samples were exhibited in fig. S5A. The x-ray photoelectron spectroscopy (XPS) measurements confirmed the removal of low-molecular weight species (fig. S5B) and enabled the valence states of Te and Se to be assigned (Fig. 2, M and N). No signals from Na 1s were detected in any of the analyzed samples (fig. S5B), indicating that dialysis effectively removed all low-molecular weight water-soluble impurities from the TeSe nanomaterials. The binding energies at ~ 573 and ~ 583 eV showed the typical peaks assigned to the Te $3d_{5/2}$ and $3d_{3/2}$ regions, respectively (Fig. 2M). Additional peaks were slightly shifted from the two Te $3d_{5/2}$ and $3d_{3/2}$ peaks (Fig. 2M), which exhibited relatively low amplitude intensities and decrease in strength by increasing the Se ratio. For the Se XPS spectra, the intensities of the typical Se $3d_{5/2}$ and $3d_{3/2}$ regions increased when the Te:Se ratio was decreased from TeSe(1:0.25) to TeSe(1:1) (Fig. 2N). In addition to principal peaks, peak intensity with chemical shifts in the various TeSe samples also increased along increasing the Se ratio.

Neat Te nanowires exhibited a broadband absorption at 200 to 1200 nm (Fig. 2O). Peaks at 282 and 560 nm attributed to a direct

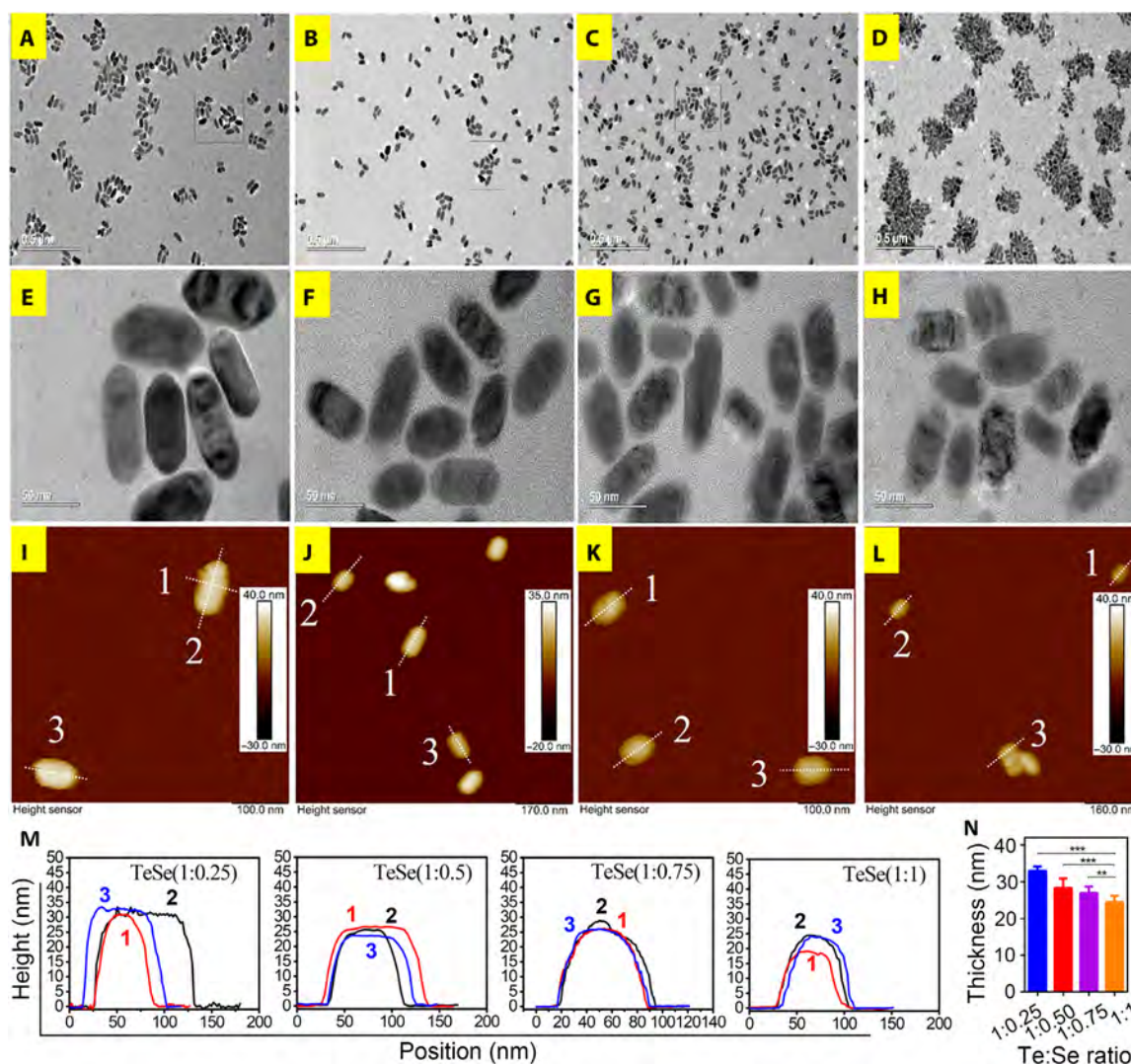


Fig. 1. Morphology of TeSe nanomaterials. TEM images (A to H), AFM images, and corresponding height line profiles (I to L) for TeSe-based nanostructures. TEM images: Low magnification of samples synthesized with a PVP concentration of 2 mg/ml and fixed initial Te contents [(A) TeSe(1:0.25), (B) TeSe(1:0.5), (C) TeSe(1:0.75), and (D) TeSe(1:1)] and their corresponding high-magnification images [(E) TeSe(1:0.25), (F) TeSe(1:0.5), (G) TeSe(1:0.75), and (H) TeSe(1:1)]. AFM images obtained from (E) to (H): (I) TeSe(1:0.25), (J) TeSe(1:0.5), (K) TeSe(1:0.75), and (L) TeSe(1:1). Height profiles were obtained from (I) to (L). (M) Thickness of three typical nanoparticles of TeSe(1:0.25), TeSe(1:0.5), TeSe(1:0.75), and TeSe(1:1). (N) Statistical analysis of the thickness between TeSe(1:0.25), TeSe(1:0.5), TeSe(1:0.75), and TeSe(1:1). $n = 10$ nanoparticles for each group, Student's t test. $**P < 0.01$, and $***P < 0.001$; mean \pm SD.

transition from a valence band to a conduction band, accompanied with a forbidden direction transition of Te. The TeSe samples showed enhanced absorption in the ultraviolet (UV) region. Along increasing the Se content, the absorption peak in the UV region progressively blue-shifted, leading to a gradual decrease of the Te direct bandgap (E_g). In addition, the TeSe samples exhibited moderate absorptions in both the visible and near-infrared regions. At a power density of 1.0 W/cm^2 , all the TeSe nanomaterials exhibited excellent photothermal properties under illumination with 808-nm light in comparison to water (Fig. 2P). TeSe(1:1) had a photothermal conversion efficiency (η) of up to 99.1% (Fig. 2Q). In addition, good photothermal stability was also observed for TeSe(1:0.25) and TeSe(1:1) (Fig. 2R). High η values, a favorable photothermal stability, and polymer-tailed nanostructures pose TeSe nanomaterials a promising photothermal agent and a drug carrier platform for cancer therapy. Together, these results demonstrated the 2D Te core–Se shell structure, the

physical characteristics, the light absorbance properties, and the light-to-heat conversion effectiveness of TeSe nanomaterials.

In vitro and in vivo biosafety

After Se doping, the toxicity of the TeSe nanomaterials both in vitro and in vivo was assessed. The Te nanomaterials exhibited obvious toxicity at a concentration of 100 parts per million (ppm), whereas the TeSe nanomaterials were completely nontoxic even at a high concentration of 400 ppm (Fig. 3A and fig. S6, A and B). Te nanoparticles typically degraded in water within 6 days (Fig. 3, B and C), and TeO_3^{2-} was determined to be the degradation product (fig. S6C). In contrast, the TeSe nanomaterials were very stable (Fig. 3D). At the 1:1 ratio of TeSe, nanomaterials were stable for a month without a sign for degradation (Fig. 3, E and F). Injection (1.5 mg/kg) of Te nanoparticles into mice resulted in low survival rates (Fig. 3A). By contrast, TeSe(1:1) at the dose of 6.0 mg/kg did not induce any

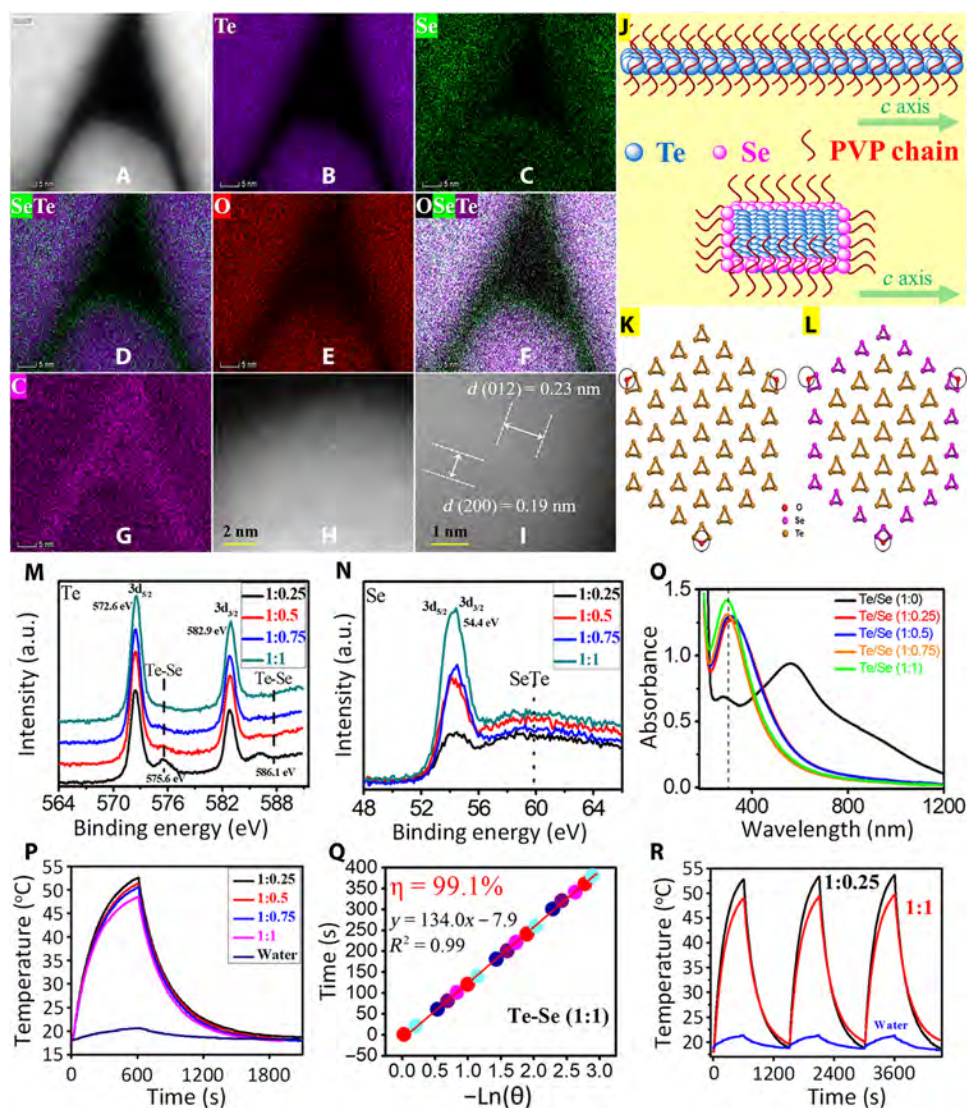


Fig. 2. Physical properties of TeSe nanomaterials. (A) TEM image showing three nanoparticles and space in between. (B) Corresponding Te-rich element image. (C) Se-rich element image. (D) Integrated Te and Se element image. (E) O-rich element image. (F) Integrated Te, Se, and O element image. (G) C-rich element image. HRTEM image showing (H) crystals with atomic arrangement on surfaces and amorphous regions at edges and (I) atomic arrangement on its surface. (J) Proposed schematic illustrating the arrangements of Te and Se atoms in the presence of PVP chains and a nanowire and an oval shape to explain the relationship of Te and Se in the 1D and 2D geometry, respectively. (K and L) The simulated oxidized atomic structures for (K) $\text{Te}_{111}\text{O}_3$ and (L) $\text{Se}_{54}\text{Te}_{57}\text{O}_3$. The red, pink, and orange color represents the oxygen (O), selenium (Se), and tellurium (Te), respectively. (M and N) X-ray photoelectron spectra: Te 3d and Se 3d. a.u., arbitrary units. (O) Ultraviolet-visible (UV-vis) absorption spectra in the range of 200 to 1200 nm; solvent: deionized water. (P) Photothermal properties [200 parts per million (ppm), 808 nm, 1.0 W/cm²]. (Q) Photothermal conversion efficiency (η) of TeSe(1:1) sample. (R) Photothermal stability (808 nm, 1.0 W/cm²).

lethality and other adverse effects including body weight (Fig. 3, H and I). The *in vitro* and *in vivo* biocompatibilities of TeSe nanomaterials are comparable to that of well-established 2D nanomaterials such as BP and titanium nanosheets (35, 36). Together, these data demonstrated that all the TeSe nanomaterials were biocompatible, stable, and nontoxic. Other parameters including hematological and organ toxicity analyses further supported this conclusion (fig. S6, D to F).

In vivo tumor-targeting efficiency of the 2D TeSe nanomaterials

Altering the Te:Se ratio during the synthetic process was demonstrated to result in TeSe nanoheterojunctions of different sizes. The Te:Se ratio also affected the photothermal conversion efficiency (η).

Investigation of the accumulative efficiency and *in vivo* distribution of different TeSe nanomaterials was an important aspect for improving therapeutic efficacy and minimizing adverse effects. Using a hepatocellular carcinoma (HCC) mouse model, we observed that the TeSe(1:1) nanomaterials exhibit the highest accumulating efficiency in the tumor compared with TeSe(1:0.75), TeSe(1:0.5), TeSe(1:0.25), and the cy7 solution (Fig. 4A). In addition, the peak accumulation time was 4 hours after injection (Fig. 4B), and the fluorescence intensity of each organ was imaged 24 hours after injection. Among the TeSe nanomaterials, TeSe(1:1) was observed to accumulate most efficiently in the tumors with an efficiency of about 33%, which exceeded most previously reported nanomaterials (Fig. 4, C and D). Another important aspect was that the TeSe(1:1) nanomaterial was

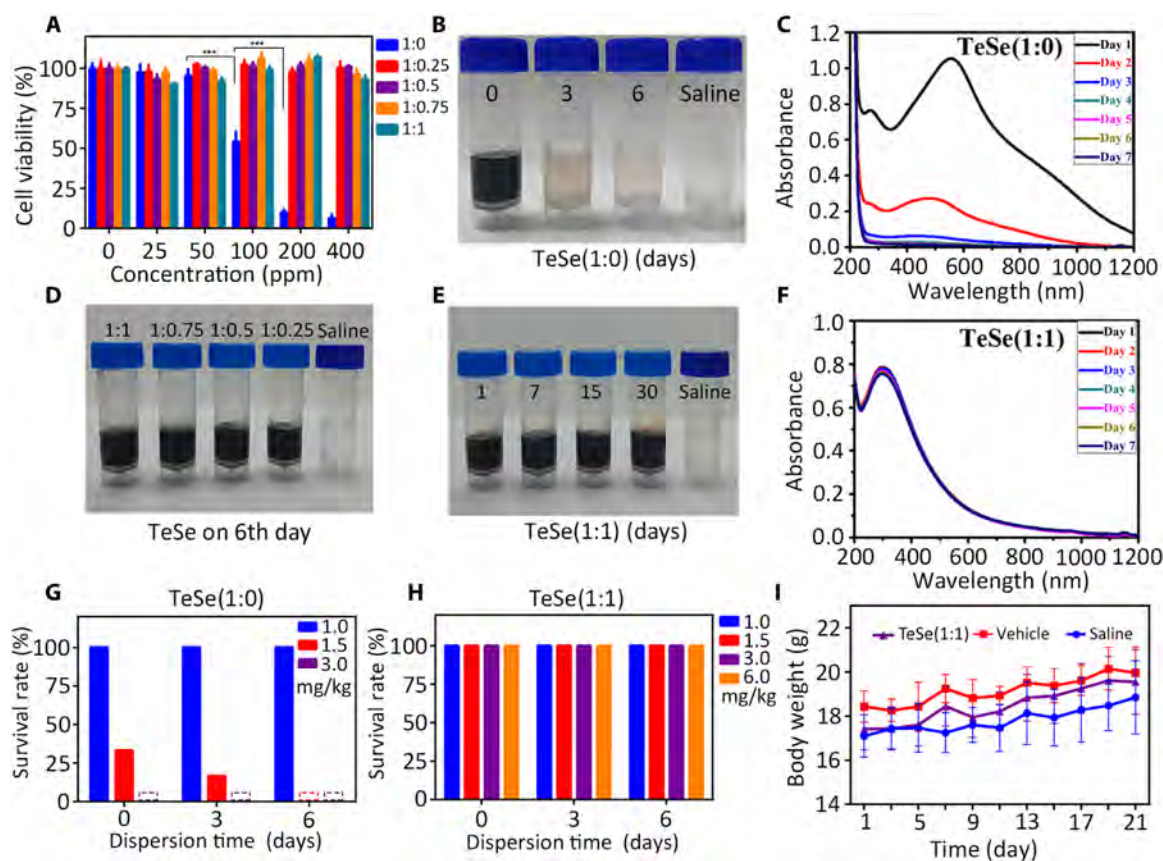


Fig. 3. Biosafety assessment of TeSe nanomaterials. (A) Assessment of cell viabilities of SMMC-7721 cells. $n = 3$ biological samples, Student's t tests. $***P < 0.001$, mean \pm SD. (B) Photographs of neat Te nanomaterials in saline (1000 ppm) at various storage times (0, 3, and 6 days). (C) Absorbance curve of Te dispersions after indicated days. (D) Photographs of TeSe-based samples (1000 ppm) [TeSe(1:1), (1:0.75), (1:0.5), and (1:0.25)] in saline after 6-day storage. (E) Photographs of TeSe(1:1) (250 ppm) in saline with various storage times (1, 7, 15, and 30 days). (F) Absorbance curve of TeSe(1:1) dispersions after indicated days. (G) Survival rate of mice after injection of neat Te nanomaterials dispersed for various durations (0, 3, and 6 days) at different injection dosages (1.0, 1.5, and 3.0 mg/kg). (H) Survival rates of mice after injection of TeSe(1:1) stored for various durations (0, 3, and 6 days) and at different injection dosages (1.0, 1.5, 3.0, and 6.0 mg/kg). (I) Body weight of mice after injection of saline, vehicle (PVP solution), and TeSe(1:1).

specifically accumulated in tumor tissues relative to other tissues and organs (Fig. 4, E and F). Among all tested ratios, TeSe at the ratio of 1:1 gave the uniform size of nanoparticles, high efficiency of PTT conversion, and high tumor accumulation. On the basis of these properties, we chose TeSe(1:1) nanoparticles as the best candidate for cancer therapy. Although the mechanism underlying tumor-specific targeting warrants further investigation, this property would potentially maximize therapeutic outcome without causing overt adverse effects.

In vitro and in vivo PTT efficiency

The light-to-heat conversion efficiency was determined from the aforementioned results. Tumor cell death was evaluated in concentration-, irradiation time-, and power density-dependent ways. At 100 ppm, all ratios of TeSe including TeSe(1:0.25), TeSe(1:0.5), TeSe(1:0.75), and TeSe(1:1) induced nearly 100% tumor cell death, which was far more potent than Te nanomaterials (Fig. 5A and fig. S7, A and B). These results suggest that Se doping resulted in significantly augmented photothermal efficiency, and in the range from 1:0.25 to 1:1, the photothermal effect of TeSe nanomaterials was well maintained. As a representative, TeSe(1:1) at a concentration of 100 ppm

for 2-min irradiation resulted in significantly reduced cell viability (Fig. 5B). In addition, tumor cell death was observed at a power density of 0.5 W/cm^2 (Fig. 5C). Fluorescence assays further supported these results (fig. S7C). In conclusion, these data indicate that the 2D TeSe nanomaterials exhibit effective antitumor effects at very low dosage levels without causing any adverse effects.

To further evaluate the anticancer efficacy in vivo, we studied therapeutic efficacy in preclinical models with human HCC and mouse lung cancer. Because TeSe(1:1) and TeSe(1:0.5) nanomaterials had a similar in vitro photothermal effect, but with a polarized tumor-targeting efficiency, we chose these two ratios as a pair for further anticancer studies. Temperature changes during PTT were measured. Results showed that TeSe(1:1) generated PTT of 60°C and TeSe(1:0.5) of $\sim 50^\circ\text{C}$ (Fig. 5, A and B, and fig. S8A). After laser treatment, mouse tumor volume and body weight were measured every second day. At day 17, tumor-bearing mice were anesthetized and euthanized. Mouse body weight of four groups was indistinguishable (Fig. 5C and fig. S8B). In contrast, the vehicle-treated control tumors grew rapidly (Fig. 5D and fig. S8C). Unexpectedly, tumors in the TeSe(1:0.5) group regressed sharply but rebounded rapidly, and tumors in the TeSe(1:1) group were ablated. Most tumors in the TeSe(1:1) group

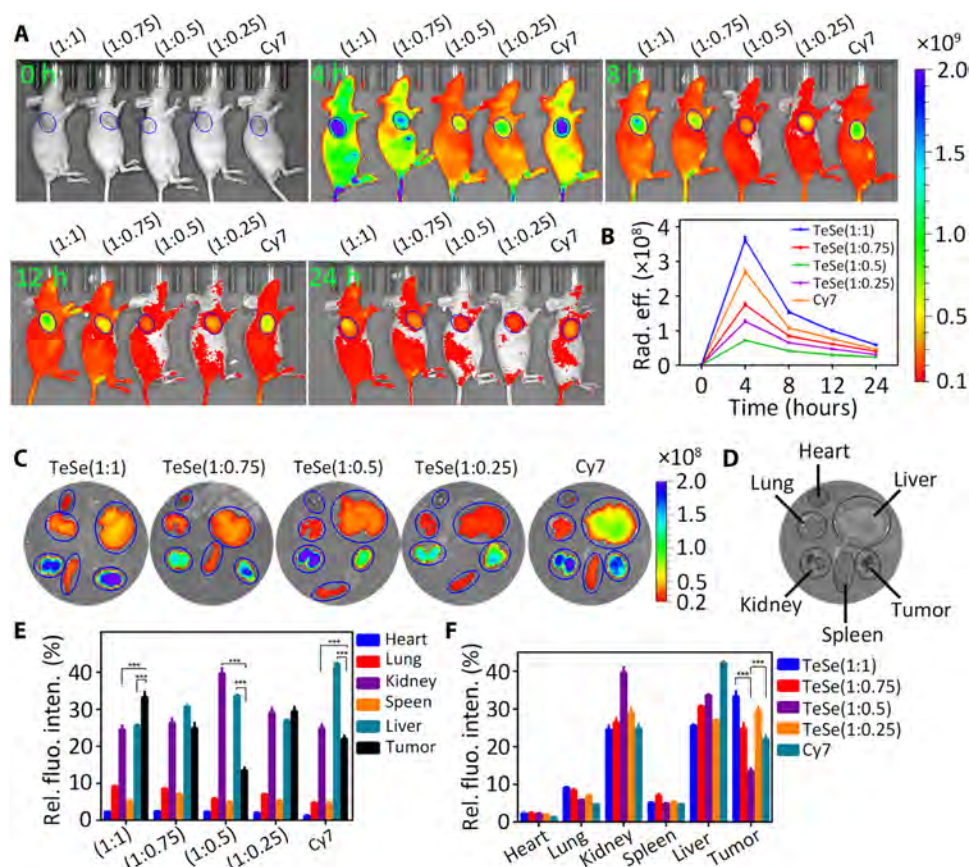


Fig. 4. Tumor-targeting efficiency exploration. A549 tumor-bearing mice were intravenously injected with the TeSe nanomaterials (2 mg/kg), loaded with the same amount of dye cy7. (A) At the indicated time points, the fluorescence intensities of the tumor sites were measured and (B) the time-dependent intensity was calculated. (C to F) At 24 hours after injection, tumors and major organs were isolated. (C) The graphic shows the fluorescence intensities of the heart, lung, kidney, spleen, tumor, and liver. (D) Illustration of the relative positions of the organs and tumors in (C). (E) Relative biodistribution in different tissues of each nanomaterial type and (F) vice versa. $n = 3$ mice, Student's t tests. *** $P < 0.001$; mean \pm SD.

were cured without further progression after long-term observation (Fig. 5, E and F). These data demonstrated that TeSe(1:1) was the most suitable TeSe nanomaterial for tumor therapy. Together, our results demonstrate that the PTT-generated high temperature is the primary driving factor for the potent antitumor effects, which are determined by both the photothermal effect and tumor-targeting efficiency of the nanomaterial.

TME changes after PTT

After PTT, we investigated the TME changes by analyzing the cellular components in response to treatment. Because TeSe(1:1)-based PTT was highly efficient, we barely observed the remaining tumors. To investigate the TME changes that could be helpful for developing combinational therapy in the future, we treated the tumors with TeSe(1:0.5)-based PTT, in which condition a small part of the tumor cells could survive. As shown, we found significant reduction of Ki67⁺ tumor cell proliferation, increase of terminal deoxynucleotidyl transferase-mediated deoxyuridine triphosphate nick end labeling-positive (TUNEL⁺) cellular apoptosis, regression of CD31⁺ vasculatures, and increase of CA9⁺ hypoxia signals in TeSe(1:0.5)-PTT-treated tumors (Fig. 6, A to F). Furthermore, tumor-associated macrophages (Iba1⁺) were decreased, implying that the antitumor immune response was also altered. The data indicate that hyperthermia

effectively induces tumor cell death and substantially alters TME. The impact of TeSe(1:0.5)-PTT on TME alteration may also imply potential functional consequences of cancer metastasis and therapeutic responses of existing anticancer drugs. These interesting aspects warrant further investigation.

DISCUSSION

In this study, we are aiming to resolve critical issues that hamper clinical implications of 2D nanomaterials. Development of 2D nanomaterials for cancer therapy has to fulfill several criteria, including no or minimal adverse effects, high anticancer efficacy, biocompatibility, superlative pharmacokinetics, and tumor targeting. At this time of writing, these major obstacles for developing 2D nanomaterials toward clinical use have not been resolved. We have fabricated a novel nanomaterial of 2D TeSe lateral heterojunction that have several unique features: (i) nontoxic nanomaterials, (ii) uniformity in morphology, (iii) relative high accumulation in tumors, (iv) highly stable, and (v) efficient light-to-heat conversion. Systemic delivery of this nontoxic TeSe nanomaterial in tumor-bearing mice produced an astounding antitumor effect, leading to a curative approach. Furthermore, delivery of the anticancer TeSe nanomaterial at an optimal ratio to animals did not result in any notable adverse effects.

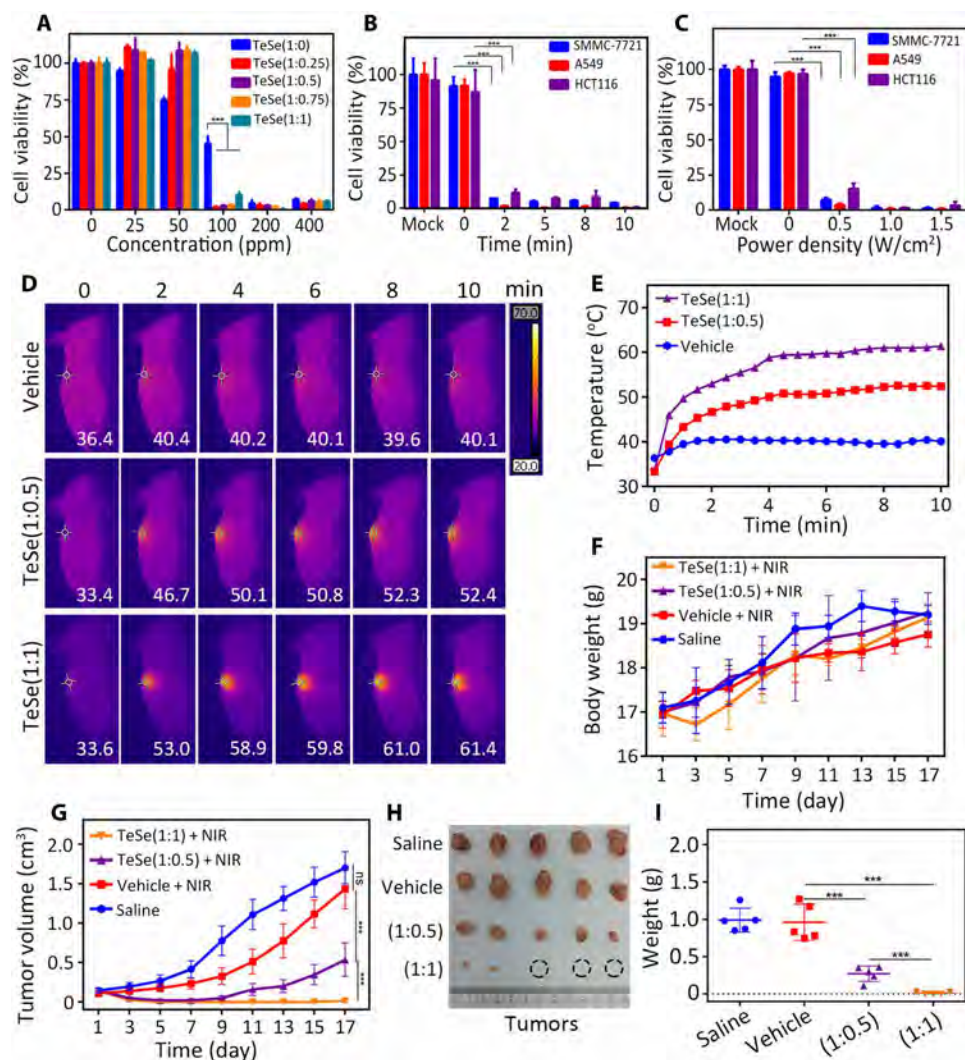


Fig. 5. In vitro and in vivo PTT. (A) Concentration-dependent PTT assays with SMMC-7721 cells at the indicated concentrations (808 nm, 1.0 W/cm², 10 min). Statistical analysis was performed between TeSe(1:0) and TeSe(1:0.25), TeSe(1:0.5), TeSe(1:0.75), or TeSe(1:1). $n = 3$, Student's t tests. $***P < 0.001$. (B) Time-dependent PTT assays. SMMC-7721 cells were treated for the indicated time (100 ppm, 808 nm, 1.0 W/cm²). $n = 3$, Student's t tests. $***P < 0.001$. (C) Power density-dependent PTT assay. SMMC-7721 cells were treated at the indicated power densities (100 ppm, 808 nm, 10 min). "Mock" refers to experiments without any treatment. Cell viabilities were determined by cholecystokinin 8 (CCK8) assays. In vivo anticancer efficacy of TeSe-based PTT is shown. $n = 3$, Student's t tests. $***P < 0.001$. (D) Temperatures at the tumor sites during the laser irradiation as a function of treatment type. (E) Real-time monitoring of the temperature changes of (D). (F to I) After treatment, the (F) body weight and (G) tumor volume were monitored every second day. At day 17, the mice were euthanized and (H) the tumors were isolated and (I) weighed. $n = 5$ mice, Student's t tests. $***P < 0.001$. Data were shown as means \pm SD. ns, nonsignificant.

We provide compelling evidence to demonstrate the uniform, stable, and nontoxic features of the TeSe nanomaterials. Although the neat nanomaterial made of Te alone is toxic, coating with Se completely ablates the toxic profile of Te. Moreover, the size of nanoparticles of TeSe lateral heterojunction can be justified by altering the ratio between Te and Se. Among all the investigated ratios, Te:Se at 1:1 produces uniform and oval-shaped nanoparticles that give rise to high light-to-heat conversion. At this optimal ratio for maximal production of thermal energy, the Te:Se heterojunctions are completely nontoxic. Another interesting finding is that systemic delivery of Te:Se nanomaterials in tumor-bearing mice results in high accumulation in tumor tissues relative to other healthy tissues and organs. Although the mechanism underlying tumor targeting is not understood, it at least not simply reflects the high blood perfusion

in tumors. According to our experiences and other published literatures, other 2D nanomaterials do not seem to have tumor-specific accumulation of nanomaterials. We would carefully speculate several possibilities for specific tumor accumulation, including (i) tumor cells (malignant cells are the highly proliferative cell population, and their gene expression profiling is highly altered relative to their adjacent healthy stromal cells or healthy cell from which they originated; probably, some of these proteins bind to TeSe nanomaterials, leading to retention of nanoparticles), (ii) stromal cells (tumor stromal cells including inflammatory cells, vascular cells, and fibroblasts are abundant cellular components in tumors, and they may retain TeSe nanomaterials by endocytosis or other mechanisms such as specific receptor-mediated uptakes), and (iii) hypoxia (tumors often experience hypoxia, and accumulation of

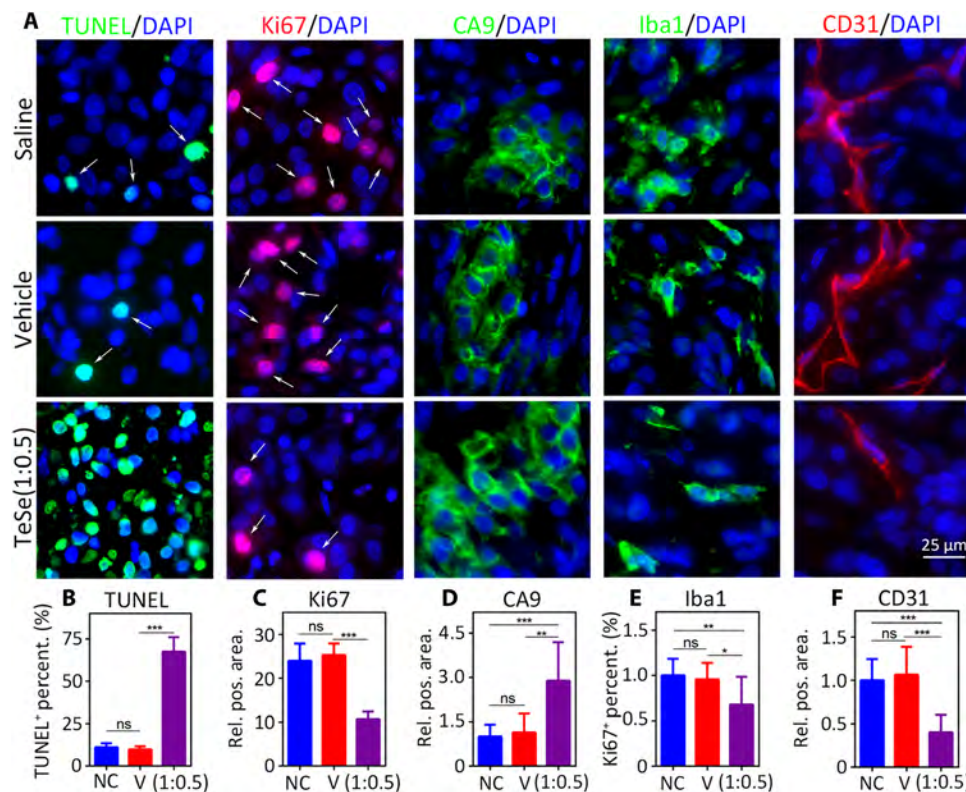


Fig. 6. Changes of TME after PTT. Tumors were isolated 3 days after PTT and subjected to paraffin section for immunofluorescence staining of DNA breaks (TUNEL), Ki67, CA9, Iba1, and CD31. (A) Representative imaging of the changes in the tumor environment. DAPI, 4',6-diamidino-2-phenylindole. (B to F) Statistical analyses as a function of parameter type, such as (B) DNA breaks by TUNEL, (C) Ki67, (D) CA9, (E) Iba1, and (F) CD31. $n > 8$ fields from five tumors, Student's t tests. * $P < 0.05$, ** $P < 0.01$, and *** $P < 0.001$. Data were shown as means \pm SD. Scale bar, 25 μ m.

TeSe nanomaterials in tumors could be partially mediated by a hypoxia-regulated mechanism; hypoxia is a consequence of rapid growth tumors, which is accompanied by altered cancer cell metabolism and behaviors such as metastasis and extracellular matrix remodeling). However, in this study, hyperthermia indiscriminately destroys cancer cells and stromal cellular components, including tumor vasculature, inflammatory cells, stromal fibroblasts, and lymphocytes. In this condition, the residual cancer cells may not readily adapt to the new microenvironment and there is a window for the combinational therapy with pH- or hypoxia-responsive drugs (37). It has been suggested that tumors became more susceptible and vulnerable to chemotherapy and radiation therapy after PTT, obtaining synergistic effect when used in combination. These interesting possibilities warrant future investigation.

PTT uses the energy from the light that can be absorbed by the tissue, and the absorbance is greatly influenced by its wavelength. In this study, we use the 808-nm light of the near-infrared region. As previously reported, the penetration depth of 808-nm light in the tissue is 3.4 cm. The power density decreased sharply in the tissue; at the depth of 0.6 cm, the power density became 60% of the emission light. However, the power density was reported to be focused in the center of the light beam, avoiding off-targeting adverse effect on the surrounding tissue, which is important for its clinical translation (38). These properties make PTT favors superficial tumors and small tumors. For the superficial tumors, the PTT is readily accessible and can be used in a combinational way. For small tumors, both primary lesions and metastatic tumors, several kinds

of nanoparticles have been translated into clinical trials, treating prostate cancer and other cancers (4).

Safety is another concern for PTT against cancer. For a local tissue, long-time exposure at above 43°C is considered dangerous and would cause irreversible severe damage to the cells (3). There are regulations about laser safety, i.e., 21 CFR 1040 in the United States and IEC 60825 internationally. As to the power density, the safe acceptable limit is called maximum permissible exposure; it is usually about 10% of the dose that has a 50% chance of creating damage. For continuous exposure, laser with power above 500 mW belongs to class 4 laser, which is the highest class of laser. Class 4 lasers are allowed to be used for industry, research, eye surgery, and skin treatments. In the present study, during the irradiation course of in vivo treatment, the temperature was above 50°C and we observed skin tissue damage. Fortunately, this kind of damage was transient and was repaired within 5 days, demonstrating that the TeSe-based PTT is safe.

Although in this study we took an approach of TeSe(1:1)-PTT monotherapy for treating experimental cancers, it is highly plausible that combination therapy consisting of TeSe(1:1)-PTT monotherapy and other conventional or targeted therapeutics would produce even greater anticancer effects. For example, combination of TeSe(1:1)-PTT with chemotherapy and radiation therapy would likely produce synergistic or additive effects owing to the multifarious anticancer mechanisms. Because our TeSe(1:1)-PTT monotherapy has already produced a curative effect in our experimental model, it would be difficult to see additional anticancer effects in a combination setting.

Together, our findings have provided an exciting possibility for approaching clinical practice with anticancer nanomaterials. We expect that either alone or in combination with other therapeutics, TeSe(1:1)-PTT would certainly shed a new light toward a curative approach for treating various cancers.

MATERIALS AND METHODS

Synthesis of TeSe nanomaterials

The TeSe-based nanomaterials were synthesized by a typical hydrothermal reaction route. Briefly, a mixture of Na_2TeO_3 , Na_2SeO_3 , water, and PVP with a molecular weight of 360,000 was added to a Teflon-lined stainless steel autoclave and completely dissolved. Next, hydrazine monohydrate ($\text{N}_2\text{H}_4 \cdot \text{H}_2\text{O}$) and ammonium hydroxide ($\text{NH}_3 \cdot \text{H}_2\text{O}$) were added into the above mixture as a reducing agent and base, respectively. The hydrothermal reaction proceeded for 3 hours at 100°C (note that the time was counted from when the reaction temperature reached 100°C). After cooling to room temperature by quenching in running water, the above mixture was dialyzed with deionized water for at least 3 days until the solution reached pH 7. The dialysis process removed the residual precursors Na_2TeO_3 and Na_2SeO_3 and excess reactants $\text{N}_2\text{H}_4 \cdot \text{H}_2\text{O}$ and $\text{NH}_3 \cdot \text{H}_2\text{O}$, which are all toxic compounds that might affect biocompatibility. The solid TeSe-based nanomaterials were obtained by a freeze-drying procedure for 48 hours. The effects of the starting molar ratios of Na_2TeO_3 (Te) to Na_2SeO_3 (Se) and the concentrations of PVP on the natures of TeSe-based nanomaterials were systematically investigated at fixed volumes of $\text{N}_2\text{H}_4 \cdot \text{H}_2\text{O}$ and $\text{NH}_3 \cdot \text{H}_2\text{O}$. Detailed synthesis information of all samples is shown in table S2.

Characterization

We examined the morphology of the as-prepared TeSe nanomaterials using a TEM (Tecnai G2 Spirit). To prepare TEM specimens, the TeSe aqueous solution was directly dropped onto carbon-supported copper wire mesh and allowed to dry for at least 3 min. The thickness of the TeSe particles was determined with an AFM (Bruker). The clear atom arrangement and elemental mapping (Te, Se, O, and C) of the TeSe samples were determined on a double spherical aberration-corrected TEM. To detect the effects of dialysis and the valence states of the TeSe samples, XPS [a PHI 5000 VersaProbe II (ULVAC-PHI) instrument] was conducted with monochromatic $\text{Al K}\alpha$ radiation. Wide scans of the TeSe samples were performed in the range of 0 to 1200 eV, and high-resolutions scans were performed for the C 1s, Na 1s, O 1s, N 1s, Te 3d, and Se 3d regions. For the TeSe-based nanomaterials, the contents of Te and Se were determined by inductively coupled plasma atomic emission spectroscopy (Optima 2100 DV, PerkinElmer). These measurements also enabled the content of the polymer PVP to be determined. The crystalline characteristics of the TeSe samples were tested by XRD and Raman measurements (Horiba LabRAM HR800). The XRD data were collected from 10° to 80° at a scanning speed of 2° min^{-1} . The Raman measurements were conducted at room temperature with an excitation wavelength of 633 nm.

Cells and reagents

SMMC-7721, A549, and HCT116 cells were obtained and cultured as previously reported (39). RPMI 1640 (HyClone), high-glucose Dulbecco's modified Eagle's medium (HyClone), fetal bovine serum (Gibco), 0.25% trypsin (HyClone), and penicillin-streptomycin

(Thermo Fisher Scientific) were used for cell cultures and passages. Goat monoclonal anti-CD31 (R&D Systems, catalog no. AF3628), rabbit monoclonal anti-Iba1 (Wako, catalog no. 019-19741), rabbit polyclonal anti-CA9 (Novus Biologicals, catalog no. NB100-417), and rat monoclonal anti-Ki67 (eBioscience, catalog no. 14-5698) were used as primary antibodies. Secondary antibodies used for paraffin section immunofluorescence were purchased from Invitrogen, including donkey anti-goat immunoglobulin G (IgG) (H + L) cross-adsorbed secondary antibody, Alexa Fluor 555; donkey anti-rabbit IgG (H + L) highly cross-adsorbed secondary antibody, Alexa Fluor 488; and goat anti-rat IgG (H + L) cross-adsorbed secondary antibody, Alexa Fluor 555. In situ cell death detection kits for TUNEL assays were purchased from Roche (catalog no. 11684795910). Cholecystokinin 8 (CCK8) assay kits were from Biotime Biotechnology. Calcein AM/PI (propidium iodide) were obtained from Sigma-Aldrich.

In vitro toxicity assays

For each cell line, cells were seeded in 96-well plates at a concentration of 6000 per well, and after adherence, the culture medium was replaced by the nanomaterial-containing media of different dispersion concentrations. At 36 hours after replacement, the cells were subjected to CCK8 assays according to the manufacturer's instructions.

In vitro PTT assays

For each cell line, cells were seeded at a concentration of 8000 cells per well in the 96-well plates, and after adherence, the culture medium was replaced by the nanomaterial-containing medium. Four hours after replacement, cells were subjected to PTT under the indicated conditions. After PTT, the culture medium was replaced with fresh medium. Cells were subjected to CCK8 and calcein AM/PI staining assays to detect the cell viability after treatment. CCK8 assays were conducted 24 hours after PTT, and calcein AM/PI assays were performed 6 hours after PTT. For concentration-dependent PTT assays, the laser power density (1.0 W/cm^2) and irradiation time (10 min) were fixed; for irradiation time-dependent assays, the concentration (100 ppm) and power density (1.0 W/cm^2) were fixed; and for power density-dependent assays, the concentration (100 ppm) and irradiation time (10 min) were fixed. All assays were performed according to the standard protocols of the manufacturer.

Animals and mouse models

All mice, including C57BL/6 and BALB/c mice, were purchased from Guangdong Medical Laboratory Animal Center (Foshan, China). The animals were maintained in standard conditions, and experiments were conducted following the protocol approved by the Laboratory Animal Ethics Committee of Shenzhen University. Female mice (at 6 to 8 weeks) were used for toxicity assays and to establish the subcutaneous tumor model. A human HCC mouse model and a human lung cancer mouse model were established in this study. To establish the HCC model, SMMC-7721 cells were prepared in phosphate-buffered saline; 2×10^6 cells were subcutaneously injected in the right flank on the back; and for lung cancer models, 4×10^6 A549 cells were injected. When the tumors grew to 100 to 200 mm^3 , the mice were subjected to tumor-targeting efficiency assessments or PTT.

In vivo toxicity assays

Female C57BL/6 mice (at 6 weeks) were intravenously injected with TeSe nanomaterials in the tail at a dosage of 5.0 mg/kg. There were five mice for each group. At 1, 7, and 21 days after injection, blood

was collected in anticoagulation tubes or procoagulation tubes to monitor the blood cells and plasma chemical parameters, respectively. The samples were processed using an automatic hematology analyzer for detection.

Tumor-targeting efficiency assays

Before injection, the dye cy7 was conjugated to the PVP-coated TeSe nanomaterials by costirring, and the conjugated nanomaterials were purified by differential centrifugations and dialysis. Thereafter, the cy7-loaded TeSe nanomaterials were dispersed in a 0.9 weight % NaCl solution, at a concentration of 1000 ppm. In addition, dye cy7 was dissolved in saline, resulting in a cy7 solution. The cy7 concentration in the nanomaterial dispersion and the saline solution are equal. To investigate the tumoral targeting efficiency, 50 μ l of the cy7 solution or the cy7-loaded TeSe nanomaterial dispersions were injected intravenously into the tail. The intensity of fluorescence at the tumor sites was monitored as a function of time using an animal living image system (PerkinElmer). To determine the relative accumulation efficiency in major organs and the tumor, at 24 hours after injection, after the living imaging of the fluorescence intensity, the mice were sacrificed, and the tumors and major organs were isolated and subjected to fluorescence intensity measurements using the same system. Three mice were used for each experimental setting, with image capturing and data processing conducted using the Living Image software.

In vivo PTT

HCC and lung cancer model mice were randomly divided into different groups (five mice for each group). Thereafter, the mice were intravenously injected with TeSe nanomaterials at a dosage of 2.0 mg/kg. At 4 hours after injection, the mice were subjected to PTT using a laser beam. The power density was set to 1.0 W/cm², with irradiation lasting 10 min on the tumor sites locally. The temperature changes during the irradiation were recorded using an infrared detector. During the entire treatment period, the tumor dimensions and body weight were recorded as a function of time. Tumor volume was calculated using the following equation: $V = L \times W^2/2$ (V , volume; L , length; W , width of the tumor). At the end of the treatment (day 17 for HCC models), the mice were euthanized, and the tumors were isolated and weighed for comparison.

TME analysis

To investigate the mechanisms by which the tumors regress after PTT, the lung cancer model mice were treated in the same manner as above, except that the TeSe(1:1) group was excluded. At 3 days after irradiation, the mice were euthanized and the tumors were isolated. The tumors were then subjected to immunohistochemistry assays, similar to a previous report (40), except with different primary and secondary antibody matches.

Statistical analyses

All data were processed using the GraphPad Prism software and presented as means \pm SD. Student's t tests were used to measure the statistical differences. The statistical values of $P < 0.05$, $P < 0.01$, and $P < 0.001$ were considered statistically significant.

SUPPLEMENTARY MATERIALS

Supplementary material for this article is available at <http://advances.sciencemag.org/cgi/content/full/6/15/eaay6825/DC1>

[View/request a protocol for this paper from Bio-protocol.](#)

REFERENCES AND NOTES

1. Y. Wang, S. Sun, Z. Zhang, D. Shi, Nanomaterials for cancer precision medicine. *Adv. Mater.* **30**, e1705660 (2018).
2. X. Huang, P. K. Jain, I. H. El-Sayed, M. A. El-Sayed, Plasmonic photothermal therapy (PPTT) using gold nanoparticles. *Lasers Med. Sci.* **23**, 217–228 (2008).
3. D. Jaque, L. Martinez Maestro, B. del Rosal, P. Haro-Gonzalez, A. Benayas, J. L. Plaza, E. Martin Rodriguez, J. Garcia Solé, Nanoparticles for photothermal therapies. *Nanoscale* **6**, 9494–9530 (2014).
4. A. C. Anselmo, S. Mitragotri, A review of clinical translation of inorganic nanoparticles. *AAPS J.* **17**, 1041–1054 (2015).
5. D. E. Dolmans, D. Fukumura, R. K. Jain, Photodynamic therapy for cancer. *Nat. Rev. Cancer* **3**, 380–387 (2003).
6. C. Xing, S. Chen, X. Liang, Q. Liu, M. Qu, Q. Zou, J. Li, H. Tan, L. Liu, D. Fan, H. Zhang, Two-dimensional MXene (Ti₃C₂)-integrated cellulose hydrogels: Toward smart three-dimensional network nanoplatforms exhibiting light-induced swelling and bimodal photothermal/chemotherapy anticancer activity. *ACS Appl. Mater. Inter.* **10**, 27631–27643 (2018).
7. B. R. Smith, S. S. Gambhir, Nanomaterials for in vivo imaging. *Chem. Rev.* **117**, 901–986 (2017).
8. H. Huang, J. F. Lovell, Advanced functional nanomaterials for theranostics. *Adv. Funct. Mater.* **27**, 1603524 (2017).
9. D. Chimene, D. L. Alge, A. K. Gaharwar, Two-dimensional nanomaterials for biomedical applications: Emerging trends and future prospects. *Adv. Mater.* **27**, 7261–7284 (2015).
10. W. Tao, X. Zhu, X. Yu, X. Zeng, Q. Xiao, X. Zhang, X. Ji, X. Wang, J. Shi, H. Zhang, L. Mei, Black phosphorus nanosheets as a robust delivery platform for cancer theranostics. *Adv. Mater.* **29**, (2017).
11. M. Qiu, D. Wang, W. Liang, L. Liu, Y. Zhang, X. Chen, D. K. Sang, C. Xing, Z. Li, B. Dong, F. Xing, D. Fan, S. Bao, H. Zhang, Y. Cao, Novel concept of the smart NIR-light-controlled drug release of black phosphorus nanostructure for cancer therapy. *Proc. Natl. Acad. Sci. U.S.A.* **115**, 501–506 (2018).
12. K. Huang, Z. Li, J. Lin, G. Han, P. Huang, Two-dimensional transition metal carbides and nitrides (MXenes) for biomedical applications. *Chem. Soc. Rev.* **47**, 5109–5124 (2018).
13. C. Cha, S. R. Shin, N. Annabi, M. R. Dokmeci, A. Khademhosseini, Carbon-based nanomaterials: Multifunctional materials for biomedical engineering. *ACS Nano* **7**, 2891–2897 (2013).
14. X. Li, J. Shan, W. Zhang, S. Su, L. Yuwen, L. Wang, Recent advances in synthesis and biomedical applications of two-dimensional transition metal dichalcogenide nanosheets. *Small* **13**, 1602660 (2017).
15. C. A. Schütz, L. Juillerat-Jeanneret, H. Mueller, I. Lynch, M. Riediker, Therapeutic nanoparticles in clinics and under clinical evaluation. *Nanomedicine* **8**, 449–467 (2013).
16. A. Kunzmann, B. Andersson, T. Thurnherr, H. Krug, A. Scheynius, B. Fadeel, Toxicology of engineered nanomaterials: Focus on biocompatibility, biodistribution and biodegradation. *BBA-Gen. Subjects* **1810**, 361–373 (2011).
17. Z. Wang, W. Zhu, Y. Qiu, X. Yi, A. von dem Bussche, A. Kane, H. Gao, K. Koski, R. Hurt, Biological and environmental interactions of emerging two-dimensional nanomaterials. *Chem. Soc. Rev.* **45**, 1750–1780 (2016).
18. J. Bourquin, A. Milosevic, D. Hauser, R. Lehner, F. Blank, A. Petri-Fink, B. Rothen-Rutishauser, Biodistribution, clearance, and long-term fate of clinically relevant nanomaterials. *Adv. Mater.* **30**, 1704307 (2018).
19. S. J. Soenen, P. Rivera-Gil, J.-M. Montenegro, W. J. Parak, S. C. De Smedt, K. Braeckmans, Cellular toxicity of inorganic nanoparticles: Common aspects and guidelines for improved nanotoxicity evaluation. *Nano Today* **6**, 446–465 (2011).
20. P. Hoet, B. Legiest, J. Geys, B. Nemery, Do nanomedicines require novel safety assessments to ensure their safety for long-term human use? *Drug Saf.* **32**, 625–636 (2009).
21. R. Li, L. Zhang, L. Shi, P. Wang, MXene Ti₃C₂: An effective 2D light-to-heat conversion material. *ACS Nano* **11**, 3752–3759 (2017).
22. N. Hao, L. Li, F. Tang, Roles of particle size, shape and surface chemistry of mesoporous silica nanomaterials on biological systems. *Int. Mater. Rev.* **62**, 57–77 (2016).
23. G. Yang, S. Z. F. Phua, A. K. Bindra, Y. Zhao, Degradability and clearance of inorganic nanoparticles for biomedical applications. *Adv. Mater.* **31**, 1805730 (2019).
24. E. B. Eherding, F. Chen, W. Cai, Biodegradable and renal clearable inorganic nanoparticles. *Adv. Sci.* **3**, 1500223 (2016).
25. M. N. O'Brien, M. R. Jones, C. A. Mirkin, The nature and implications of uniformity in the hierarchical organization of nanomaterials. *Proc. Natl. Acad. Sci. U.S.A.* **113**, 11717–11725 (2016).
26. Y. Ma, B. Li, S. Yang, Ultrathin two-dimensional metallic nanomaterials. *Mater. Chem. Front.* **2**, 456–467 (2018).
27. D. de Melo-Diogo, C. Pais-Silva, D. R. Dias, A. F. Moreira, I. J. Correia, Strategies to improve cancer photothermal therapy mediated by nanomaterials. *Adv. Healthc. Mater.* **6**, (2017).
28. X. Tang, W. Liang, J. Zhao, Z. Li, M. Qiu, T. Fan, C. S. Luo, Y. Zhou, Y. Li, Z. Guo, D. Fan, H. Zhang, Fluorinated phosphorene: Electrochemical synthesis, atomistic fluorination, and enhanced stability. *Small* **13**, 1702739 (2017).

29. J. Ji, X. Song, J. Liu, Z. Yan, C. Huo, S. Zhang, M. Su, L. Liao, W. Wang, Z. Ni, Y. Hao, H. Zeng, Two-dimensional antimonene single crystals grown by van der Waals epitaxy. *Nat. Commun.* **7**, 13352 (2016).
30. Z. He, Y. Yang, J.-W. Liu, S.-H. Yu, Emerging tellurium nanostructures: Controllable synthesis and their applications. *Chem. Soc. Rev.* **46**, 2732–2753 (2017).
31. W. Huang, Y. Huang, Y. You, T. Nie, T. Chen, High-yield synthesis of multifunctional tellurium nanorods to achieve simultaneous chemo-photothermal combination cancer therapy. *Adv. Funct. Mater.* **27**, 1701388 (2017).
32. Y. Lin, Y. Wu, R. Wang, G. Tao, P.-F. Luo, X. Lin, G. Huang, J. Li, H.-H. Yang, Two-dimensional tellurium nanosheets for photoacoustic imaging-guided photodynamic therapy. *Chem. Commun.* **54**, 8579–8582 (2018).
33. W.-J. Lan, S.-H. Yu, H.-S. Qian, Y. Wan, Dispersibility, stabilization, and chemical stability of ultrathin tellurium nanowires in acetone: Morphology change, crystallization, and transformation into TeO₂ in different solvents. *Langmuir* **23**, 3409–3417 (2007).
34. Y. Zhou, Y. Bai, H. Liu, X. Jiang, T. Tong, L. Fang, D. Wang, Q. Ke, J. Liang, S. Xiao, Tellurium/Bovine serum albumin nanocomposites inducing the formation of stress granules in a protein kinase R-dependent manner. *ACS Appl. Mater. Interfaces* **10**, 25241–25251 (2018).
35. J. Shao, H. Xie, H. Huang, Z. Li, Z. Sun, Y. Xu, Q. Xiao, X. F. Yu, Y. Zhao, H. Zhang, H. Wang, P. K. Chu, Biodegradable black phosphorus-based nanospheres for in vivo photothermal cancer therapy. *Nat. Commun.* **7**, 12967 (2016).
36. Z. Xie, S. Chen, Y. Duo, Y. Zhu, T. Fan, Q. Zou, M. Qu, Z. Lin, J. Zhao, Y. Li, L. Liu, S. Bao, H. Chen, D. Fan, H. Zhang, Biocompatible two-dimensional titanium nanosheets for multimodal imaging-guided cancer theranostics. *ACS Appl. Mater. Interfaces* **11**, 22129–22140 (2019).
37. C. Qian, J. Yu, Y. Chen, Q. Hu, X. Xiao, W. Sun, C. Wang, P. Feng, Q.-D. Shen, Z. Gu, Light-activated hypoxia-responsive nanocarriers for enhanced anticancer therapy. *Adv. Mater.* **28**, 3313–3320 (2016).
38. D. E. Hudson, D. O. Hudson, J. M. Winingar, B. D. Richardson, Penetration of laser light at 808 and 980 nm in bovine tissue samples. *Photomed. Laser Surg.* **31**, 163–168 (2013).
39. C. Xing, S. Chen, M. Qiu, X. Liang, Q. Liu, Q. Zou, Z. Li, Z. Xie, D. Wang, B. Dong, L. Liu, D. Fan, H. Zhang, Conceptually novel black phosphorus/cellulose hydrogels as promising photothermal agents for effective cancer therapy. *Adv. Healthc. Mater.* **7**, 1701510 (2018).
40. H. Iwamoto, M. Abe, Y. Yang, D. Cui, T. Seki, M. Nakamura, K. Hosaka, S. Lim, J. Wu, X. He, X. Sun, Y. Lu, Q. Zhou, W. Shi, T. Torimura, G. Nie, Q. Li, Y. Cao, Cancer lipid metabolism confers antiangiogenic drug resistance. *Cell Metab.* **28**, 104–117.e5 (2018).

Acknowledgments: We thank M. Yin for the assistance on HRTEM observation in the Electron Microscopy Center of the Shenzhen University. We also acknowledge the Materials and Devices Testing Center of Graduate School at Shenzhen, Tsinghua University, especially M. Wang, for TEM observation. **Funding:** This work was supported by the Natural Science Foundation of China (grant nos. 61875138, 81701819, 61435010, 6181101252, 61671308, and 61575089), the Science and Technology Development Fund (nos. 007/2017/A1 and 132/2017/A3), the China Postdoctoral Science Foundation (grant no. 2018 M640817), the Natural Science Foundation of Guangdong Province (grant no. 2017A030310495), the Science and Technology Innovation Commission of Shenzhen (grant nos. GRCK2017082111070420, KQTD2015032416270385, JCYJ20150625103619275, and JCYJ20170811093453105), the Scientific Research Starting Foundation for the Youth Scholars of Shenzhen University (grant no. 2019107), and the Macao Special Administration Region (SAR), China. The laboratory of Y.C. is supported through research grants from the European Research Council (ERC) advanced grant ANGIOFAT (project no 250021), the Swedish Research Council, the Swedish Cancer Foundation, the Strategic Research Areas (SFO)–Stem Cell and Regeneration Medicine Foundation, the Karolinska Institutet, the Swedish Children's Cancer Foundation, the Karolinska Institutet Foundation, the Karolinska Institutet Distinguished Professor Award, the Torsten Soderbergs Foundation, the Maud and Birger Gustavsson Foundation, the Novo Nordisk Foundation–Advance grant, and the Knut and Alice Wallenberg's Foundation. **Author contributions:** Y.C., H.Z., and L.L. supervised the study and helped analyze the data and revise the manuscript. S.C. designed and conducted the biological experiments and wrote the manuscript. C.X. designed and conducted the nanomaterial synthesis and characterization and wrote part of the manuscript. Other authors offered help during the experiment conduction and data analysis. The authors also acknowledge the support from Instrumental Analysis Center of Shenzhen University (Xili Campus). **Competing interests:** The authors declare that they have no competing interests. **Data and materials availability:** All data needed to evaluate the conclusions in the paper are present in the paper and/or the Supplementary Materials. Additional data related to this paper may be requested from the authors.

Submitted 10 July 2019
 Accepted 14 January 2020
 Published 8 April 2020
 10.1126/sciadv.aay6825

Citation: S. Chen, C. Xing, D. Huang, C. Zhou, B. Ding, Z. Guo, Z. Peng, D. Wang, X. Zhu, S. Liu, Z. Cai, J. Wu, J. Zhao, Z. Wu, Y. Zhang, C. Wei, Q. Yan, H. Wang, D. Fan, L. Liu, H. Zhang, Y. Cao, Eradication of tumor growth by delivering novel photothermal selenium-coated tellurium nanoheterojunctions. *Sci. Adv.* **6**, eaay6825 (2020).

Eradication of tumor growth by delivering novel photothermal selenium-coated tellurium nanoheterojunctions

Shiyu Chen, Chenyang Xing, Dazhou Huang, Chuanhong Zhou, Bo Ding, Ziheng Guo, Zhengchun Peng, Dou Wang, Xi Zhu, Shuzhen Liu, Zhen Cai, Jieyu Wu, Jiaqi Zhao, Zongze Wu, Yuhua Zhang, Chaoying Wei, Qiaoting Yan, Hongzhong Wang, Dianyuan Fan, Liping Liu, Han Zhang and Yihai Cao

Sci Adv 6 (15), eaay6825.
DOI: 10.1126/sciadv.aay6825

ARTICLE TOOLS

<http://advances.sciencemag.org/content/6/15/eaay6825>

SUPPLEMENTARY MATERIALS

<http://advances.sciencemag.org/content/suppl/2020/04/06/6.15.eaay6825.DC1>

REFERENCES

This article cites 38 articles, 2 of which you can access for free
<http://advances.sciencemag.org/content/6/15/eaay6825#BIBL>

PERMISSIONS

<http://www.sciencemag.org/help/reprints-and-permissions>

Use of this article is subject to the [Terms of Service](#)

Science Advances (ISSN 2375-2548) is published by the American Association for the Advancement of Science, 1200 New York Avenue NW, Washington, DC 20005. The title *Science Advances* is a registered trademark of AAAS.

Copyright © 2020 The Authors, some rights reserved; exclusive licensee American Association for the Advancement of Science. No claim to original U.S. Government Works. Distributed under a Creative Commons Attribution NonCommercial License 4.0 (CC BY-NC).